Thermal conductivity anisotropy and grain structure in $Ge_2Sb_2Te_5$ films

Jaeho Lee,[1,a)] Zijian Li,[1] John P. Reifenberg,[1] Sangchul Lee,[2] Robert Sinclair,[2] Mehdi Asheghi,[1] and Kenneth E. Goodson[1]
[1]*Department of Mechanical Engineering, Stanford University, Stanford, California 94305, USA*
[2]*Department of Material Science Engineering, Stanford University, Stanford, California 94305, USA*

(Received 18 January 2011; accepted 5 March 2011; published online 19 April 2011)

Although lateral thermal conduction in $Ge_2Sb_2Te_5$ (GST) films can influence the performance of phase change memory (PCM), there are no data available for the in-plane thermal conductivity. This work measures both the in-plane and the out-of-plane thermal conductivities for the amorphous, face-centered-cubic, and hexagonal-close-packed phases of GST using two independent techniques. For crystalline GST, we report anisotropy favoring out-of-plane conduction by up to 54%, which varies with annealing time. Scaling arguments indicate that the anisotropy may be due to the thermal resistance of amorphous regions near grain boundaries. This explanation is consistent with transmission electron microscopy images showing columnar grains and amorphous phase at grain boundaries. © *2011 American Institute of Physics*. [doi:10.1063/1.3573505]

I. INTRODUCTION

Phase change memory (PCM) promises high read/write/erase speeds and scalability, simultaneously offering nonvolatility and bit alterability. The thermal conduction properties of $Ge_2Sb_2Te_5$ (GST) and related compounds govern the performance of PCM devices.[1] There have been many studies of the thermal conductivity normal to GST films,[2–10] but the in-plane thermal conductivity or the possibility of conductivity anisotropy has received very little attention. Thermal conductivity anisotropy in thin films can result from electron or phonon scattering on film interfaces, partially oriented grains, inhomogeneous material quality, or molecular orientation in the case of polymers.[11–13] Lateral thermal conduction in GST films can affect the cross talk in high density cells[14] and the programming current of PCM devices in particular to novel lateral designs.[15–17]

This work measures both the in-plane and the out-of-plane thermal conductivities of GST films in various annealing conditions. We use two experimental methods. The suspended structure in Fig. 1 induces joule heating in the lateral direction and measures the in-plane thermal conductivity. The heat confinement within thin films also allows the heat capacity measurement of GST films. The on-substrate structure with variable width heaters in Fig. 2 measures the out-of-plane thermal conductivity and the conductivity anisotropy collectively using the 3ω method. The two measurement techniques validate the results for each other and offer consistent information of the thermal conductivities. Transmission electron microscopy (TEM) observations provide clues to the grain structure and the mechanism for the thermal conductivity anisotropy found in this manuscript.

II. EXPERIMENTAL METHODS

A. In-plane conductivity measurements using a suspended structure

Samples for the suspended structure are prepared with double-side-polished silicon wafers. First, 460-nm-thick thermal oxides are grown on both sides to offer mechanical support. A 440 nm-thick-GST film is deposited on the front side by rf magnetron sputtering in argon with a pressure of 5 mT at the room temperature. A 70-nm-thick Si_3N_4 layer covers the GST for electrical passivation. Fifty-nanometer-thick Pt bridges are patterned on the surface by lift-off. The wafers are then coated with a 7-μm-thick SPR-220 photoresist on the front side and baked for 5 h at 90 °C. As the baked photoresist protects the patterned structures, HF etches the thermal oxide on the backside. The deep reactive ion etching (DRIE) removes the full thickness of silicon and creates 200 μm $\times$ 3200 μm trenches. High selectivity between Si and SiO_2 (100:1) minimizes overetch during DRIE. The thickness of SiO_2 is verified by the spectroreflectometry. Acetone dissolves the protective photoresist on the front side and completes the fabrication of free-standing layers including SiO_2, GST, and Si_3N_4. Reference samples are prepared by identical processing steps with no GST.

The suspended structure allows steady-state measurements of the in-plane thermal conductivity. With dc power supply, a Pt heater provides joule heating in the lateral direction, and adjacent metal bridges measure the temperature rise at various locations. The thermometer distances x_A and x_B vary from 20 to 160 μm. Each thermometer uses a four-probe electrical resistance method and calibrates the temperature coefficient of resistance with a sensitivity of 0.4 mV/K. The thermal conduction resistance of the suspended structure is much smaller than the other heat transfer paths. Convection and radiation losses can be further minimized by controlling the suspended window size ($x_C < 200$ μm) and the peak temperature rise of the heater ($T_{peak} < 10$ °C).

[a)]Electronic mail: zeost@stanford.edu. FAX: (650) 723-7657.

FIG. 1. (Color online) Cross-sectional schematic of suspended structure measuring the in-plane thermal conductivity and the heat capacity. Each metal bridge can serve as heater and thermometer. The distances between heater and thermometers (x_A and x_B) vary from 20 to 160 μm to provide lateral temperature distribution. Not drawn to scale.

The in-plane thermal conductivity of the GST film, $k_{x,\mathrm{GST}}$, is calculated from

$$\frac{1}{\Delta T_1}-\frac{1}{\Delta T_2}=\left(\frac{2d_{\mathrm{GST}}k_{x,\mathrm{GST}}L}{\Delta x}\right)\frac{1}{P}, \tag{1}$$

where d_{GST} is the film thickness, L is the heater length, P is the heating power, $\Delta x = x_A + x_B$ is the distance between the two thermometers, $\Delta T_1 = T_{A,1} - T_{B,1}$ is the difference in temperatures measured at x_A and x_B from the samples with GST, and $\Delta T_2 = T_{A,2} - T_{B,2}$ is the difference in temperatures measured from the sample with no GST. The reference sample accounts for the contributions of the SiO_2 and Si_3N_4 layers. A linearly fitted slope of the inverse temperature on the left-hand side of the equation and the inverse power extracts the in-plane thermal conductivity of GST film.

B. In-plane and out-of-plane conductivity measurements using variable width heaters

Samples for the variable width heaters are prepared on a silicon substrate. First, a 3-μm-thick thermal oxide is grown to provide significant lateral spreading from narrow heaters. A-600-nm thick GST film is deposited by the same processing with the suspended structure. Similarly the Si_3N_4 and Pt layers are deposited on the GST, and the variable width heaters are patterned by lift-off. The limits of the heater width (2–100 μm) are defined by heating power considerations and the resolution of the lithography system. Reference structures with no GST are prepared on the same substrate to improve differential measurements. The differential measurements determine the temperature drop exclusively across the GST film by canceling the effects of substrate and passivation layers.

The variable width heaters measure the thermal conductivity of GST using the 3ω method. A metal line transmits current at frequency ω and generates joule heating at 2ω. The resulting change in the electrical resistance creates a 3ω component in the voltage across the heater. A circuitry of differential amplifiers extracts the 3ω voltage and a lock-in amplifier (SR830) detects the in-phase signal with high sensitivity. The 3ω voltage captures the amplitude of temperature rise in response of underlying materials including the GST film. A further explanation of the 3ω method can be found elsewhere.[18–20]

A recursive matrix formulation solves the heat-conduction equation considering the anisotropy in the multilayer structure. Successive matrix multiplications account for the temperature response of each layer from a temporally modulated heat source at the surface of the top layer,[21] which yields

$$\Delta T_{\mathrm{avg}} = \frac{P}{2\pi L}\int_0^\infty \frac{B^+(k)+B^-(k)}{B^-(k)A^+(k)-B^+(k)A^-(k)}\frac{\mathrm{sinc}^2(kb)}{k_{n,z}\gamma_n}dk, \tag{2}$$

$$\gamma_n = \sqrt{\eta_n k^2 + i\omega/D_n}. \tag{3}$$

The average temperature rise ΔT_{avg} is for the top metal layer, b is the heater half-width, the parameters κ and D_j refer to the thermal conductivity and diffusivity of layer j in the out-of-plane direction, η_j is its anisotropy ratio, and $B^+(k)$, $B^-(k)$, $A^+(k)$, and $A^-(k)$ are dimensionless parameters determined by the matrix recursions.[22] The expression $\mathrm{sinc}^2(kb)/\gamma_n$ captures the effects of anisotropy. The anisotropy ratio influences γ_n most strongly at high spatial frequencies when k is large compared to ω/D. The integrand and the average temperature are most sensitive to the anisotropy ratio when the heater is narrow and the film thickness is large.

The heaters of widths larger than 60 μm measure the out-of-plane thermal conductivity of GST films, and the heaters of widths smaller than 10 μm measure their anisotropy ratio. Using the measured out-of-plane thermal conductivity (k_z), the mathematical model fits the anisotropy ratio ($\eta = k_x/k_z$) and the in-plane thermal conductivity (k_x). Figure 3 shows the temperature response of a 2-μm-wide heater on the 600–nm-thick GST film.

The 3ω method maximizes the measurement sensitivity of thin films by modulating the frequencies, 300–1500 Hz, where the characteristic diffusion depth is large compared to the film thicknesses but smaller than the substrate thickness. The temperature response in higher frequency domain

FIG. 2. (Color online) Cross-sectional schematic of variable width heaters measuring the out-of-plane thermal conductivity and the conductivity anisotropy. The width of metal bridges varies from 2 to 100 μm to separate contributions of the out-of-plane and the in-plane thermal conductions. Reference structure has no GST underneath the heater. Not drawn to scale.

FIG. 3. (Color online) The analytical solution determines the best fit frequency responses using the out-of-plane thermal conductivity and anisotropy ratio as fitting parameters. The measured temperature amplitude decays with increasing frequency because of reduced thermal diffusion depth and increased thermal mass effect of thin films.

becomes sensitive to the heat capacity of thin films. Given the frequency limit of the lock-in amplifier, the on-substrate measurement is not sensitive to the heat capacity of GST films.

Measurements on the 3 μm thermal oxide validate the experimental system. The thermal conductivity (1.45 W m^{-1} K^{-1}), heat capacity, (1.99×10^6 J m^{-3} K^{-1}) and anisotropy ratio ($\eta = 1$) of the SiO_2 layer match closely with literature values.[19]

C. Heat capacity measurements using a suspended structure

The suspended structure becomes sensitive to the heat capacity of GST films using harmonic Joule heating. An infinitely long bridge assumption with high measurement frequency provide the in-plane temperature distribution

$$\theta(x,t) = \frac{q''l}{2\sqrt{2}k_{\text{eff}}}\exp\left(-\frac{x}{1}\right)\cos\left(\omega t - \frac{x}{1} - \frac{x}{4}\right), \qquad (4)$$

where $\theta(x,t) = T(x,t) - T_0$ is the temperature elevation at location x and time t, q'' is the heat flux generated by the central heater, and k_{eff} is the effective thermal conductivity of the multilayer membrane. The phase difference of transient temperature responses at different locations depends on the thermal diffusion length, l, which is defined as

$$l = \sqrt{\frac{\alpha_{\text{eff}}}{\omega}}, \qquad (5)$$

where α_{eff} is the effective thermal diffusivity of the multilayer membrane. The heat capacity of the GST films can be derived from the effective thermal diffusivity by subtracting the contributions of the SiO_2 and Si_3N_4 layers. The measurement temperature controlled by a hot chuck ranges from 20 to 150 °C.

D. Microstructural characterization

The GST films for all measurements are initially prepared as amorphous. The temperatures of processing steps are kept under 110 °C to avoid any crystallization. The face-centered-cubic (fcc) and the hexagonal-close-packed (hcp) samples are made by postannealing. The temperature dependent x-ray diffraction (XRD) peaks in Fig. 4 indicate the phase of GST samples annealed at various temperatures.

FIG. 4. (Color online) XRD peaks of GST films collected using Cu $K\alpha$ radiation. The fcc lattice constant $a = 6.01$ Å and the hcp lattice contants $a = 4.26$ Å, $c = 17.65$ Å are estimated by Bragg's law. Average crystallite sizes 20–30 nm for the fcc and the hcp phases are estimated from the full-width at half-maximum.

A hot stage inside the x-ray diffractometer controls the temperature from 26 to 300 °C with an increment of 10 °C. The crystallization to the fcc phase occurs at 110 °C and the transition to the hcp phase begins at 200 °C. At first, the fcc and the hcp crystals coexist.[23] The GST film transforms into the full hcp phase after annealing for 30 min at 200 °C. Annealing time governs the degree of crystallization and consequently influences the intensities of XRD peaks. The crystalline samples for the suspended structure are prepared by annealing them at 150 and 260 °C for 30 min each. The crystalline samples for the variable width heaters are prepared by annealing them at 150 °C for 30, 60, and 120 min and at 200 °C for 30 min.

TEM reveals the grain structure of GST films that may be responsible for the thermal conductivity anisotropy measured in this manuscript. Figure 5(a) shows the columnar grains of 20–30 nm wide for the crystalline GST film annealed at 150 °C for 30 min. The TEM images indicate that the crystallization is triggered by heterogeneous nucleation at the interfaces and the grains are grown normal to the substrate. Similarly, a number of studies report that the nucleation of crystalline GST begins at the surface as a spherical shape and further proceeds by the growth through thickness of the film.[24–27] A periodic arrangement of amorphous phase is found at grain boundaries of the crystalline GST film. The shape of amorphous regions follows the texture of columnar grains.

III. RESULTS AND DISCUSSION

Figure 6 plots the in-plane thermal conductivities measured by the suspended structure including 0.18 ± 0.01 W m^{-1} K^{-1} for the amorphous GST film, 0.49 ± 0.03

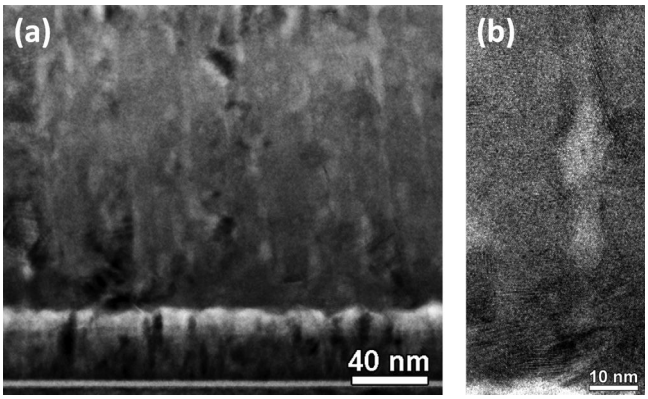

FIG. 5. Cross-sectional TEM images show the columnar grain structure for the GST film annealed at 150 °C for 30 min. The magnified image (b) shows a 10-nm-wide amorphous region remains at the grain boundary.

$W\,m^{-1}\,K^{-1}$ for the fcc GST film annealed at 150 °C, and 1.03 ± 0.07 $W\,m^{-1}\,K^{-1}$ for the hcp GST film annealed at 260 °C. The uncertainties in film thickness d_{GST}, heater length L, and heating power P are 2%, 2.5%, and 1%, respectively. The major sources of uncertainty are convection and radiation heat losses that can be as large as 10% error in the thermal conductivity data.

The out-of-plane thermal conductivity measured by the variable width heaters using the 3ω method shows an increase from 0.17 ± 0.01 $W\,m^{-1}\,K^{-1}$ for the amorphous phase to 0.56 ± 0.03, 1.01 ± 0.06, and 1.25 ± 0.08 $W\,m^{-1}\,K^{-1}$ for the crystalline phases with annealing temperatures of 150, 200, and 260 °C, respectively. These data are consistent with our past work[7] and literature values[2–10] for the thermal conductivity of GST films. Measurements performed with the heaters of widths larger than 60 μm can isolate heat spreading with an error of less than 1%. The measured thermal conductivity may deviate from the intrinsic properties due to the presence of thermal boundary resistance (TBR). Our previous work using the thickness dependence reports the TBR between GST and SiO_2 layers as 2.5×10^{-8} $m^2\,K^{-1}\,W^{-1}$.[28] This TBR value yields 1.8% error in the measurement of the out-of-plane thermal conductivity. The major source of uncertainty for the 3ω measurements stems from the temperature calibration of resistive thermometers, which is as large as 5%.

FIG. 6. (Color online) The out-of-plane and the in-plane thermal conductivities of GST films measured using the two methods described in this manuscript. X-ray diffraction data show that the samples annealed at 150, 200, and 260 °C (30 min each) become polycrystalline.

FIG. 7. (Color online) The thermal conductivity anisotropy ratios (in-plane divided by out-of-plane conductivity) measured using the experimental structures after annealing for 30 min at different temperatures. The GST samples annealed above 200 °C contain hexagonal crystals.

Figure 7 compares the anisotropy ratios measured by two different methods as a function of annealing temperature. The anisotropy ratios are either determined directly from the variable width heaters or combining the results of the suspended structure and a wide heater. The measurement results are consistent within 0.65–0.8 anisotropy for the crystalline GST films that are annealed for 30 min.

The uncertainty of the out-of-plane thermal conductivity measurement strongly influences the uncertainty of the anisotropy ratio estimation during the mathematical fitting. The 2% error in the temperature amplitude in Fig. 3 results in nearly 20% error in the anisotropy ratio estimation. Another source of uncertainty is the unknown thermal boundary resistance (TBR) between the GST and the passivation layers. Only when the TBR is 10 times larger than the estimate does the uncertainty in data analysis become significant. The measurement data without considering the TBR sets an upper bound of the anisotropy ratio.

The heat capacity for the crystalline GST film is measured to be $1.27 \pm 0.02 \times 10^6$ $J\,K^{-1}\,m^{-3}$ and does not show any temperature dependence from 20 to 150 °C. This trend is consistent with Debye model for heat capacity at the high temperature limit as the Debye temperature (T_D) of GST, which is around 100 K.[29] At the high temperature end where $T \gg T_D$, the heat capacity can be simplified as

$$C \approx 3nk_B, \tag{6}$$

where C is volumetric heat capacity, n is atomic number density, and k_B is Boltzmann constant. The atomic number density of GST is reported as 3.09×10^{22} cm^{-3} from the Rutherford backscattering spectrometry.[5] Equation (6) then predicts the heat capacity of GST as 1.28×10^6 $J\,K^{-1}\,m^{-3}$. The good agreement between the Debye model and the experiment result indicates that the electron contribution of heat capacity in crystalline GST is very small.

In columnar structure, phonons in the in-plane direction scatter more frequently to the grain boundaries when their mean free path is comparable to the grain size. The full-width at half-maximum of x-ray peaks in Fig. 4 estimates the average crystallite size as 20–30 nm for the fcc and hcp GST films. Similar values for crystalline GST films are found in literature.[30,31] The mean free path of phonons (l) can be estimated by the kinetic theory ($k = Cvl/3$) measured values of thermal conductivity (k) and heat capacity (C) predict the phonon mean free path as 1 nm at most. The sound velocity ($v = 3$ nm/ps) of GST is referenced from literature.[5] Because the estimated mean free path is much smaller than the grain size, phonon scattering on grain boundaries is not sufficient to explain the conductivity anisotropy.

The high resolution TEM image in Fig. 5(b) reveals the presence of amorphous phase in the grain boundaries of crystalline GST. These phase impurities may originate from the residues of crystal nucleation via annealing. The thermal conductivity of the amorphous phase is only 30% of that of the crystalline phase. Phonon scattering on the textured phase impurity can explain the anisotropy favoring out-of-plane conduction for the crystalline GST films.

Figure 8 reports the annealing time dependence of the thermal conductivities. The thermal conductivities increase significantly at the onset of annealing at 150 °C due to the crystallization of amorphous GST. The in-plane thermal conductivity continues to increase until 60 min of annealing, whereas the out-of-plane thermal conductivity remains constant within the error bars. After 60 mins, the thermal conductivities show no appreciable change.

The variation of the thermal conductivity anisotropy in Fig. 8 correlates with varying fraction of the phase impurities over time. The volume fraction of the crystalline region (X_c) and the amorphous region ($X_a = 1 - X_c$) during isothermal transformation can be modeled according to the Johnson–Mehl–Avrami–Kolmogrov (JMAK) equation,[32,33]

$$X_c = 1 - \exp(-Kt^m), \tag{7}$$

where m is the Avrami exponent and K is a rate constant. The Avrami exponent is set to 2 assuming interface-controlled one- dimensional growth nucleation at a constant rate. Many authors have found similar values from their studies.[26,27,32,33] The rate constant is determined from the best fit to the data. The JMAK equation implicates that the fraction of phase impurity decays exponentially with time. A simple resistor model of amorphous phase (R_a) and crystalline phase (R_c) can capture the time varying fraction of phase impurity and its impact on the conductivities of GST for both directions.

Assuming the amorphous regions are textured uniformly across the thickness of GST, the resistance in the in-plane and the out- of-plane directions can be modeled with the crystal fraction (X_c) through relations

$$R_x = X_c R_c + (1 - X_c) R_a, \tag{8}$$

$$R_z = \left(\frac{X_c}{R_c} + \frac{1 - X_c}{R_a} \right)^{-1}, \tag{9}$$

where R_x and R_z are the inverse of the conductivities in the in-plane and the out-of-plane directions, respectively. The amorphous and the crystalline resistors are in series for the in-plane direction and in parallel for the out-of-plane direction. This model associates the columnar grains and the phase impurity observed in Fig. 5. Using the contrast in the thermal conductivity data for the amorphous and the crystalline GST films, the model successfully captures the annealing time dependence in Fig. 8. The best fit model predicts that the thermal conductivity anisotropy ratio can be as large as 0.6 when the sample is annealed for 20 min.

A number of studies have reported that the JMAK equation satisfies the crystallization behavior of GST using similar models.[25–27,31–33] Optical reflectivity[32] and electrical resistivity[25–27] measurements also have shown strong dependence on the degree of crystallization and annealing time. Their works consistently show that the measurement results plateau as GST films are fully crystallized after a long anneal.

IV. CONCLUSIONS

This work presents the design and fabrication of experimental structures sensitive to lateral thermal conduction in GST films. The thermal conductivity anisotropy favoring the out-of-plane conduction is found in crystalline GST and varies with annealing time. We report the thermal resistance of amorphous regions near grain boundaries as the mechanism for the conductivity anisotropy. The JMAK equation accounts for the time varying fraction of phase impurities in the thermal conductivity data.

Controlled processing conditions can engineer the microstructure and conduction path depending on the geometry of the PCM cell. The thermal conductivity anisotropy can work in favor to reduce the programming power or to prevent the cross-talk between adjacent cells. Understanding the conduction behaviors improves the quality of device

FIG. 8. (Color online) The out-of-plane and the in-plane thermal conductivities of GST film measured as a function of annealing time. The amorphous GST is annealed at 150 °C for each time-duration. The in-plane thermal conductivity increases and then plateaus after 60 min of annealing. The out-of-plane thermal conductivity shows no appreciable change after the crystallization.

simulations, and their dependence on the processing condition can have large influence on the design of novel phase change memory.

ACKNOWLEDGMENTS

The authors appreciate support from Intel Corporation, the Semiconductor Research Corporation through Contract No. 2009-VJ-1996, and the National Science Foundation through Grant No. CBET-0853350. The authors also acknowledge the Stanford Nanofabrication Facility (SNF) and the Stanford Nanocharacterization Laboratory (SNL) for their support in fabrication and SEM measurement.

[1]J. P. Reifenberg, D. L. Kencke, and K. E. Goodson, IEEE Electron Device Lett. **29**, 10 (2008).
[2]C. Peng, L. Cheng, and M. Mansuripur, J. Appl. Phys. **82**, 4183 (1997).
[3]E. K. Kim, S. I. Kwun, S. M. Lee, H. Seo, and J. G. Yoon, Appl. Phys. Lett. **76**, 3864 (2000).
[4]V. Giraud, J. Cluzel, V. Sousa, A. Jacquot, A. Dauscher, B. Lenoir, H. Scherrer, and S. Romer, J. Appl. Phys. **98**, 013520 (2005).
[5]H.-K. Lyeo, D. G. Cahill, B.-S. Lee, J. R. Abelson, M.-H. Kwon, K.-B. Kim, S. G. Bishop, and B.-k. Cheong, Appl. Phys. Lett. **89**, 151904 (2006).
[6]M. Kuwahara, O. Suzuki, Y. Yamakawa, N. Taketoshi, T. Yagi, P. Fons, T. Fukaya, J. Tominaga, and T. Baba, Microelectron. Eng. **84** 1792 (2007).
[7]J. P. Reifenberg, M. A. Panzer, S.-B. Kim, A. M. Gibby, Y. Zhang, S. Wong, H.-S. Philip Wong, E. Pop, and K. E. Goodson, Appl. Phys. Lett. **91**, 111904 (2007).
[8]W. P. Risk, C. T. Rettner, and S. Raoux, Appl. Phys. Lett. **94**, 101906 (2009).
[9]R. Fallica, J. Battaglia, S. Cocco, C. Monguzzi, A. Teren, C. Wiemer, E. Varesi, R. Cecchini, A. Gotti, and M. Fanciulli, J. Chem. Eng. Data **54**, 1698 (2009).
[10]J.-L. Battaglia, A. Kusiak, V. Schick, A. Cappella, C. Wiemer, M. Longo, and E. Varesi, J. Appl. Phys. **107**, 044314 (2010).
[11]J. E. Graebner, S. Jin, G. W. Kammlott, J. A. Herb, and C. F. Gardinier, Nature **359**, 401 (1992).
[12]K. Kurabayashi, M. Asheghi, M. Touzelbaev, and K. E. Goodson, IEEE J. MicroElectroMech. Syst. **8**, 180 (1999).
[13]W. L. Liu, T. Borca-Tasciuc, G. Chen, J. L. Liu, and K. L. Wang, J. Nanosci. Nanotechnol. **1**, 39 (2001).
[14]A. Pirovano, A. L. Lacaita, A. Benvenuti, F. Pellizzer, S. Hudgens, and R. Bez, IEDM Tech. Dig. **2003**, 699 (2003).
[15]M. Lankhorst, B. Ketelaars, and R. Wolters, Nat. Mater. **4**, 347 (2005).
[16]Y. Yin, A. Miyachi, D. Niida, H. Sone, and S. Hosaka, Jpn. J. Appl. Phys., Part 1 **45**, 3238 (2006).
[17]F. Merget, D. H. Kim, P. Haring Bolivar, and H. Kurz, Microsyst. Technol. **13**, 169 (2007).
[18]D. G. Cahill, Rev. Sci. Instrum. **61**, 802 (1990).
[19]Y. S. Ju and K. E. Goodson, J. Appl. Phys. **85**, 7130 (1999).
[20]C. Dames and G. Chen, Rev. Sci. Instrum. **76**, 124902 (2006).
[21]J. H. Kim, A. Feldman, and D. Novotny, J. Appl. Phys. **86**, 3959 (1999).
[22]A. Feldman, High Temp.-High Press. **31**, 293 (1999).
[23]I. Friedrich, V. Weidenhof, W. Njoroge, P. Franz, and M. Wuttig, J. Appl. Phys. **87**, 130 (2000).
[24]S. W. Ryu, J. H. Oh, J. H. Lee, B. J. Choi, W. Kim, S. K. Hong, C. S. Hwang, and H. J. Kim, Appl. Phys. Lett. **92**, 142110 (2008).
[25]P. La Fata, F. Torrisi, S. Lombardo, G. Nicotra, R. Puglisi, and E. Rimini, J. Appl. Phys. **105** (2009).
[26]S. Lombardo, E. Rimini, M.G. Grimaldi, and S. Privitera, Microelectron. Eng. **87**, 294 (2010).
[27]D. Z. Hu, X. M. Lu, J. S. Zhu, and F. J. Yan, Appl. Phys. **102**, 113507 (2007).
[28]J. Lee, E. Elah Bozorg-Grayeli, Z. Li, J. P. Reifenberg, M. Asheghi, and K. E. Goodson, Proceedings of Itherm, 2010, 5501412, pp. 1–6.
[29]T. Blachowicz, M. G. Beghi, G. Guntherodt, B. Beschoten, H. Dieker, and M. Wuttig, J. Appl. Phys. **102**, 093519 (2007).
[30]Y. Park, J. Lee, M. Youm, and Y. Kim, Jpn. J. Appl. Phys. **44**, 326 (2005).
[31]I. Yang, K. Do, H.-J. Chang, D.-H. Ko, and H. Sohn, J. Electrochem. Soc. **157**, H483 (2010).
[32]T. H. Jeong, M. R. Kim, H. Seo, S. J. Kim, and S. Y. Kim, J. Appl. Phys. **86**, 774 (1999).
[33]G. Ruitenberg, A. K. Petford-Long, and R. C. Doole, J. Appl. Phys. **92**, 3116 (2002).